J Mater Sci (2011) 46:6603–6608
DOI 10.1007/s10853-011-5609-2

Novel insight into microstructural evolution of phase-separated Cu–Co alloys under influence of forced convection

Y. K. Zhang · J. Gao · L. L. Wei · M. Kolbe · T. Volkmann · D. Herlach

Received: 8 February 2011 / Accepted: 3 May 2011 / Published online: 12 May 2011

Abstract Cu–Co alloys of bulk compositions $Cu_{75}Co_{25}$ and $Cu_{84}Co_{16}$ were undercooled and solidified using electromagnetic levitation. Microstructure of the samples was characterized using optical microscopy, scanning electron microscopy, energy dispersive spectrometry, and micro X-ray diffraction analysis. It was found that besides a bimodal size distribution, droplets of the Co-rich L_1 phase resulting from liquid phase separation have a broad composition distribution. The bimodal size distribution of the droplets is more pronounced for the $Cu_{75}Co_{25}$ sample than for the $Cu_{84}Co_{16}$ sample, whilst the composition distribution of the droplets is broader in the $Cu_{75}Co_{25}$ sample than in the $Cu_{84}Co_{16}$ sample. The droplets were found to also have different types of substructures in the two samples. The results provide novel insight into microstructural evolution of phase-separated alloys under influence of forced convection.

Introduction

A metastable miscibility gap exists in the undercooled region of the binary Cu–Co system [1]. When a homogeneous liquid is undercooled to a binodal temperature of the miscibility gap, it will be separated into two liquids, Co-rich L_1 phase and Cu-rich L_2 phase. Such a liquid–liquid phase separation process can begin with two alternative mechanisms, i.e., nucleation of the minority phase or spinodal decomposition [2]. The former mechanism leads to a dispersed structure, whereas the latter mechanism leads to an interconnected structure. The phase boundaries of the metastable miscibility gap and phase-separated microstructure have been investigated during the past decades [3–22]. It has been verified that the metastable miscibility gap has a flat dome and that the critical point lies in the Cu-rich side of the phase diagram [14, 18, 19]. On the other hand, it has been established that phase-separated microstructure depends on bulk composition, undercooling, and cooling rate [3–17, 19–21]. Among these factors, the cooling rate plays a critical role in determining the scale of final microstructure. Slow cooling produces macroscopically segregated egg-like structures [11, 12, 14, 16, 19], whereas fast cooling prevents initial structures from coarsening [4, 7, 9, 10, 15–17, 21].

Electromagnetic levitation has often been used to undercool bulk Cu–Co samples [3, 5, 6, 12, 16]. However, levitated samples are subjected to forced convection due to a rotational component of the electromagnetic force [22]. The influence of forced convection on phase-separated microstructure of Cu–Co samples has been little investigated so far. Few recent studies showed that damping of forced convection, which was realized by utilization of a low gravity environment [23] or alternatively by imposition of a static magnetic field [24, 25], suppresses collision-induced coagulation of droplets of the minority phase, leading to a transition of droplet size distribution from a bimodal one to a quasi-monomodal one. In this study, two Cu–Co samples of Cu-rich bulk compositions were undercooled to the respective binodal temperature using electromagnetic levitation. Besides a bimodal size distribution, the Co-rich L_1 droplets resulting from liquid phase

Y. K. Zhang · J. Gao (✉) · L. L. Wei
Key Laboratory of Electromagnetic Processing of Materials, Ministry of Education, Northeastern University, Shenyang 110004, China
e-mail: jgao@mail.neu.edu.cn

Y. K. Zhang · M. Kolbe · T. Volkmann · D. Herlach
Institut für Materialphysik im Weltraum, Deutsches Zentrum für Luft- und Raumfahrt (DLR), 51170 Köln, Germany

separation were determined to have a broad distribution of chemical composition. The broad composition distribution differs from a previous finding of identical compositions, allowing us to produce novel insight into liquid phase separation and rapid solidification process of undercooled Cu–Co alloys.

Experimental

Alloys of bulk compositions $Cu_{75}Co_{25}$ and $Cu_{84}Co_{16}$ were prepared by arc-melting of elemental Cu and Co of 99.99% purity under the protection of Ar atmosphere. Each alloy had a mass of 1.2 g. They were processed using an electromagnetic levitator following similar procedures. Before levitation, one sample was inserted into the coil of the levitator, and supported with an alumina-made holder. The chamber of the levitator was evacuated to a vacuum pressure of 8×10^{-4} Pa, and backfilled with Ar of 99.999% purity to a pressure of 3×10^{4} Pa. The sample was levitated, melted, and overheated by increasing power input to the coil. The surface temperature of the sample was monitored using a single-color pyrometer. After soaking for less than 1 min, the sample was cooled by a stream of a He + 8 vol.% H_2 mixed gas. For each sample, two separated recalescence events were detected during solidification. The bulk undercooling of the samples was estimated to be larger than 200 K. Both samples had a mass loss due to evaporation of Cu. Thus, their compositions became less Cu-rich. For convenience, their starting compositions are referred to below.

The as-solidified samples were mounted in an epoxy resin. After grinding and polishing, their microstructure was examined using an optical microscope (OM) and a scanning electron microscope (SEM). For each sample, two parallel cross-sections with a distance of a few millimeters were examined. The samples were etched with an aqueous solution of $FeCl_3$ + HCl for OM investigations. They were re-polished for SEM investigations in the back-scattering mode. Elemental concentrations of micro regions were measured using an energy dispersive X-ray spectrometer (EDS) attached to the SEM. Crystal structures of phase constituents were determined by micro X-ray diffraction using Cu Kα radiation.

Results

The two samples underwent metastable liquid phase separation. As illustrated in Fig. 1, their solidification microstructure exhibits a dispersion of Co-rich droplets and Co-rich dendrites in a Cu-rich matrix. The Co-rich droplets correspond to the L_1 phase, which solidified first and retained a spherical morphology of the liquid state. The Co-rich dendrites and the Cu-rich matrix have a common origin of the L_2 phase, which solidified later than the L_1 phase did. A quantitative characterization revealed that there are differences in size distribution, chemical composition, and substructure of the Co-rich droplets between the two samples.

Figure 2 shows droplet size distribution diagrams on a logarithm-normal scale. Here a droplet size refers to an apparent radius measured in a cross-section of the samples. In order to reduce the statistical error, droplet frequencies counted over the two parallel cross-sections of each sample were added up, and normalized with respect to a sum of droplet populations. Both diagrams display a bimodal size distribution: a primary peak and a secondary peak emerge on the smaller side and on the larger side, respectively. For the $Cu_{84}Co_{16}$ sample, the primary peak is centered at $\ln(r) = 1.97$ μm with a normalized frequency of 20.4%, whereas the secondary peak is centered at $\ln(r) = 2.88$ μm with a normalized frequency of 2.2%. Here the maximum frequency of the secondary peak has an uncertainty of 0.22%, which represents a mean frequency of the droplets on the larger side. For the $Cu_{75}Co_{25}$ sample, the primary peak is centered at $\ln(r) = 1.68$ μm with a normalized frequency of 16.1%, whereas the secondary peak is centered at $\ln(r) = 2.88$ μm with a normalized frequency of 7.6%. The main differences between the samples lie in two aspects. The primary peak is higher and centered at a larger size for the $Cu_{84}Co_{16}$ sample than for the $Co_{75}Co_{25}$ sample, whereas the secondary peak is much broader and much higher for the $Co_{75}Co_{25}$ sample than for the $Cu_{84}Co_{16}$ sample.

Figure 3 shows Cu concentrations of selected droplets measured by EDS. In order to reduce the error of the data, the measurements were carried out on droplets having a size of larger than 3 μm only. A distribution of droplet composition was commonly revealed for the droplets of the two samples. In the $Cu_{84}Co_{16}$ sample, 86 droplets were measured, showing a Cu concentration ranging from 10.9 to 25.3 at.%. In the $Cu_{75}Co_{25}$ sample, 65 droplets were measured, showing a Cu concentration ranging from 17.9 to 39.0 at.%. The distribution of droplet composition is broader in the $Cu_{75}Co_{25}$ sample than in the $Cu_{84}Co_{16}$ sample. Unlike the droplet size, the Cu concentration of the droplets does not show a bimodal characteristic on a logarithm-normal scale. Small-sized droplets are the major source for the broad distribution, because they show a large scatter with respect to large-sized ones.

Figure 4 illustrates substructures of the droplets. The droplets in the $Cu_{84}Co_{16}$ sample show two types of substructures, which are denoted as A and B type, respectively. The A type has a closed periphery and a nearly segregation-free core (see Fig. 4a). The B type has an open

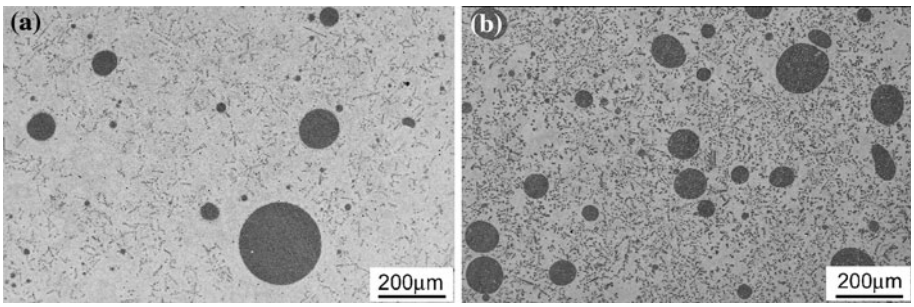

Fig. 1 Back-scattered SEM micrographs showing phase-separated microstructure of Cu–Co samples: **a** $Cu_{84}Co_{16}$ and **b** $Cu_{75}Co_{25}$

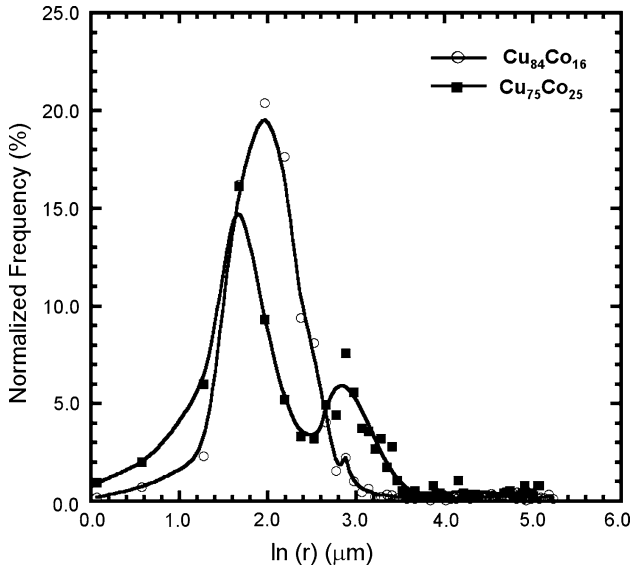

Fig. 2 Normalized frequency versus apparent radius of Co-rich droplets in Cu–Co samples. *Open circles*: $Cu_{84}Co_{16}$; *filled squares*: $Cu_{75}Co_{25}$

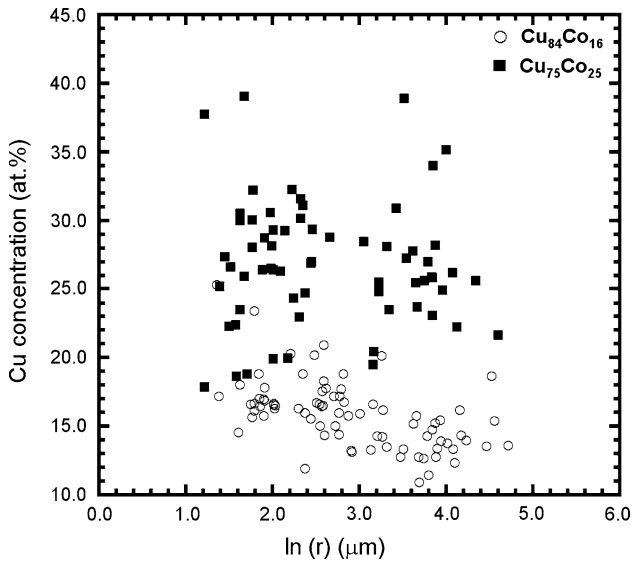

Fig. 3 EDS-measured Cu concentration versus apparent radius of Co-rich droplets in Cu–Co samples. *Open circles*: $Cu_{84}Co_{16}$; *filled squares*: $Cu_{75}Co_{25}$

periphery, and consists of fine Co-rich grains and thin Cu-rich intergranular layers (see Fig. 4b). Two other types of substructures were observed for the droplets in the $Cu_{75}Co_{25}$ sample. They are denoted as C and D type, respectively. The C type shows a dispersion of Cu-rich dots in the Co-rich matrix (see Fig. 4c), whereas the D type shows a mixture of irregular Co-rich islands and Cu-rich channels (see Fig. 4d). Similar to the C type substructure, each of the islands of the D type substructure consists of a dispersion of Cu-rich dots and rods in a Co-rich matrix. Figure 5 shows an EDS line scan of the D type substructure. The matrices of the islands have nearly constant Co concentrations within a single droplet. This is also the case for the matrices of few adjacent Co-rich droplets. These findings suggest that a chemical equilibrium is held between the L_1 droplets and the L_2 matrices.

Figure 6 illustrates micro X-ray diffraction patterns of several regions centered about large-sized droplets. The diffraction peaks are indexed to two face-centered cubic solid solutions (see Fig. 6a). A set of stronger peaks corresponds to Cu-rich solid solution, whereas a set of weaker peaks to Co-rich solid solution. The Bragg angles of the peaks of both phases vary slightly with location of the probed regions, suggesting a distribution of solute concentration. On the other hand, the peaks of the $Cu_{75}Co_{25}$ sample are shifted to lower angles with respect to those of the $Cu_{84}Co_{16}$ sample (see Fig. 6b), indicating a general difference in solute concentration of the two phases.

Discussion

Droplet size distribution

As explained elsewhere, the bimodal size distribution in phase-separated Cu–Co samples is due to diffusive growth and forced convection-induced coagulation of the L_1 droplets [23–25]. The present results show a more pronounced bimodal size distribution for the droplets of the $Cu_{75}Co_{25}$ sample than that for the droplets of the $Cu_{84}Co_{16}$ sample. It is implied that forced convection imposes a

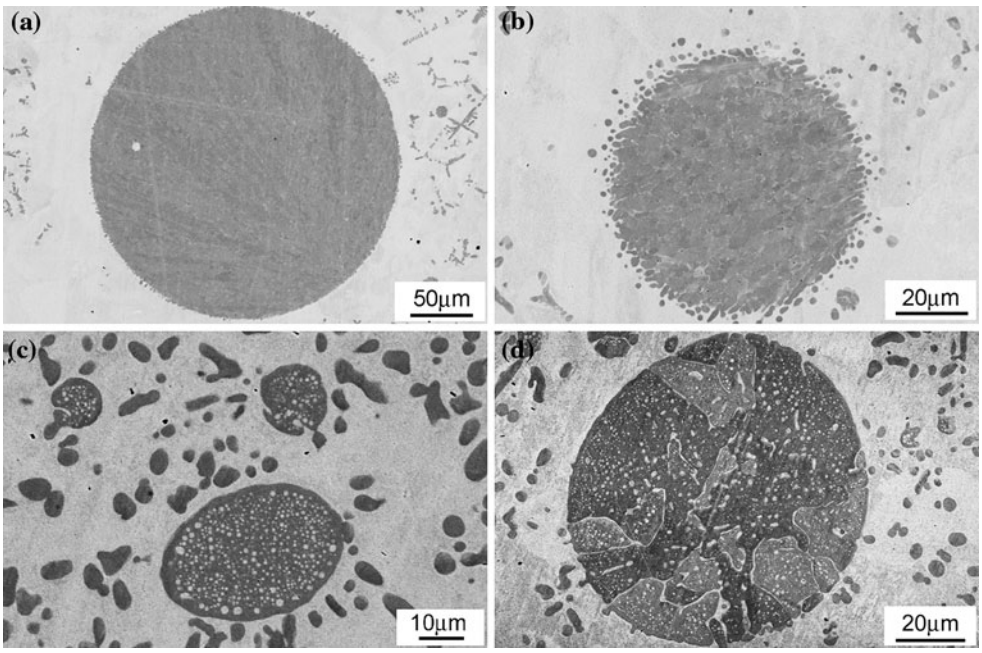

Fig. 4 Back-scattered SEM micrographs showing different types of substructures of Co-rich droplets in Cu–Co samples. **a**, **b** A type and B type substructures in the $Cu_{84}Co_{16}$ sample. **c**, **d** C type and D type substructures in the $Cu_{75}Co_{25}$ sample

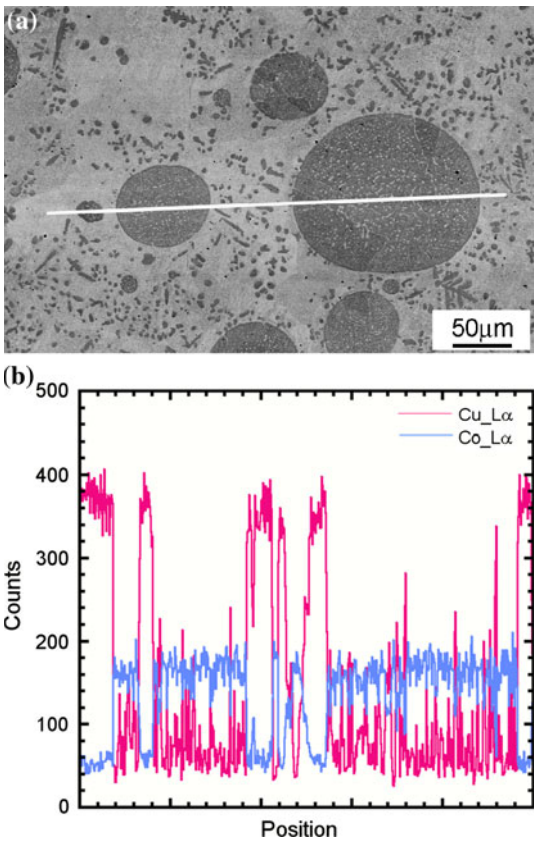

Fig. 5 EDS line scan of L_1 droplets in the $Cu_{75}Co_{25}$ sample. **a** Location and length of the line and **b** elemental concentrations along the *line* shown in **a**

greater influence on droplet coagulation in the $Cu_{75}Co_{25}$ sample. Such a difference between the two samples can be explained in terms of nucleation kinetics of the L_1 droplets during liquid phase separation. The details are given below.

A recent modeling [26] showed that the liquid/liquid interfacial energy between the L_1 and L_2 phases is much lower in the $Cu_{75}Co_{25}$ sample than in the $Cu_{84}Co_{16}$ sample (3.8 vs. 28.5 mJ/m^2) at the respective binodal temperature. We can therefore assume that the L_1 droplets have a higher nucleation rate in the $Cu_{75}Co_{25}$ sample during liquid phase separation. Since the higher nucleation rate reduces supersaturation of the L_2 matrix phase, the L_1 droplets will have a lower growth velocity in the $Cu_{75}Co_{25}$ sample than in the $Cu_{84}Co_{16}$ sample [2]. If the L_1 droplets are not coagulated with others, they will keep a smaller size. This explains why the primary peak of the droplet size distribution diagram is centered at a smaller size for the $Cu_{75}Co_{25}$ sample than for the $Cu_{84}Co_{16}$ sample. Actually, many of the L_1 droplets have been coagulated in the $Cu_{75}Co_{25}$ sample under action of forced convection. As a result, the population of small-sized droplets is reduced. This explains why the primary peak of the droplet size distribution diagram is lower for the $Cu_{75}Co_{25}$ sample than for the $Cu_{84}Co_{16}$ sample. More critically, the higher density of the L_1 droplets in the $Cu_{75}Co_{25}$ sample brings about a higher probability and a higher frequency of droplet collision driven by forced convection. Hence, the coagulated L_1 droplets have a larger population and a larger scatter in size. This explains why the secondary peak of the

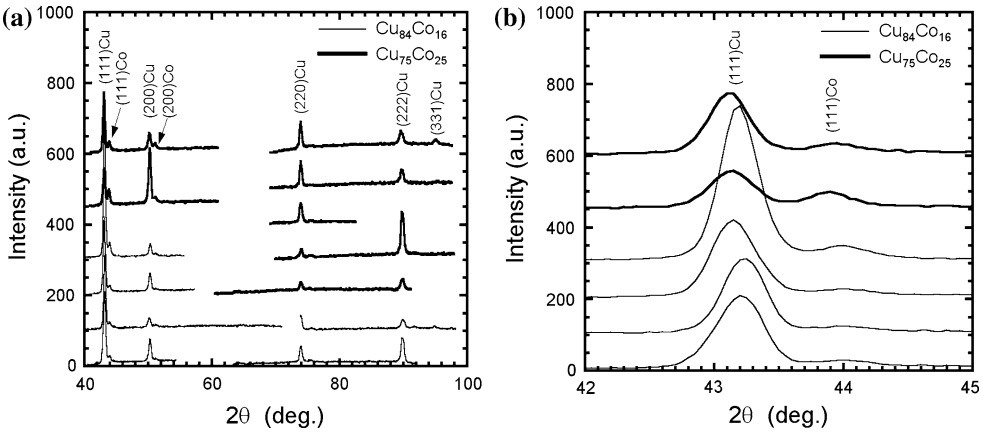

Fig. 6 Micro X-ray diffraction patterns taken at different locations of the samples. **a** Overview and **b** enlarged view of the low angle patterns

droplet size distribution diagram is broader and higher for the $Cu_{75}Co_{25}$ sample than for the $Cu_{84}Co_{16}$ sample.

Droplet composition distribution

In contrast to the previous finding of identical compositions for all droplets of the L_1 phase in a given sample [3, 5, 6, 8, 12], the present results show a broad distribution of droplet composition. This new finding explains why the early established phase boundaries of the metastable miscibility gap by measurements of droplet composition are not reliable with respect to those determined by the recent thermal analyses [14, 18]. The scatter in droplet composition was observed by Song et al. [7] for melt-spun Cu–Co samples. In the following, possible reasons for the scatter in the droplet composition are discussed by reference to the substructures of the droplets.

We suppose that a dynamic phase separation process is largely responsible for the scatter in droplet composition in the $Cu_{75}Co_{25}$ sample. According to the verified metastable miscibility gap [14, 18], Cu concentration of the L_1 droplets is high at the onset temperature of liquid phase separation. When the sample temperature decreases, new L_1 droplets with a lower Cu concentration will be nucleated. Meanwhile, the Cu concentration of the old L_1 droplets needs to be lowered in order to keep the chemical equilibrium with the L_2 matrix. There are two mechanisms for the latter event. One is by rejection of excess Cu atoms to the L_2 matrix, and the other is by nucleation and growth of L_2 droplets within the L_1 droplets in an "in situ" process. The two mechanisms are hinted at by the substructures of the L_1 droplets. As seen in Fig. 4c and d, the Co-rich rims of the substructures correspond to rejection of excess Cu atoms, whereas the dispersed Cu-rich dots in the core correspond to in situ decomposition. Because the rims are thin, the old L_1 droplets have nearly same compositions as before. Due to the presence of Cu-rich dots, the Cu concentration of the old L_1 droplets is higher than that of the freshly nucleated L_1 droplets. During continuous cooling, new L_1 droplets will become old ones, and also experience in situ decomposition. In such a way, a variety of droplet compositions are produced.

Besides the dynamic liquid phase separation, there is a second reason for the scatter in droplet composition in the $Cu_{75}Co_{25}$ sample. Considering a stochastic distribution of catalytic sites in the volume of the bulk liquid, we assume that the L_1 droplets crystallize into Co-rich solid solution in an asynchronous manner. In other words, those containing highly catalytic sites solidify at a higher temperature, and retain a high Cu concentration. The population of those droplets, however, should be small, because the released latent heat does not cause any additional and detectable recalescence event. Other L_1 droplets containing no catalytic sites or weakly catalytic sites only undergo further phase separation by rejection of excess Cu atoms during continuous cooling of the sample. Their lower Cu concentrations are frozen in through collective rapid solidification at an identical temperature. The asynchronous crystallization of the L_1 droplets is hinted at by the variable solutal concentrations of Co-rich solid solution (see Fig. 6b). In addition, previous observations of a multiple recalescence process for phase-separated Fe–Cu samples [27] provide additional evidence for this.

For the $Cu_{84}Co_{16}$ sample, Cu-rich dots are seldom seen in the matrices of the L_1 droplets (see Fig. 4a, b). It is therefore suggested that the dynamic liquid phase separation process is not the major reason for the scatter in the droplet composition. Such a situation can be understood, because the binodal of the miscibility gap is so steep in the low temperature region of the Cu–Co phase diagram that the old L_1 droplets do not need to reject too many excess Cu atoms during continuous cooling. Inversely, we suppose that the scatter in droplet composition in the $Cu_{84}Co_{16}$ sample is mainly caused by asynchronous crystallization of the droplets.

Finally, it is mentioned that the B type substructure in the $Cu_{84}Co_{16}$ sample has been observed for glass-fluxed

samples, and attributed to Marangoni convection [21]. According to the present results, such an explanation is disputable, because the Marangoni convection cannot play a role in the presence of forced convection.

Conclusion

A quantitative characterization of the phase-separated microstructure of two electromagnetically levitated samples of bulk compositions of $Cu_{84}Co_{16}$ and $Cu_{75}Co_{25}$ has revealed that besides a bimodal size distribution, the Co-rich L_1 droplets have a broad distribution of droplet composition and different types of substructures. The more pronounced bimodal size distribution for the droplets of the $Cu_{75}Co_{25}$ sample has been related to a higher nucleation rate of the L_1 droplets during liquid phase separation, which reduces the growth velocity of the droplets, but promotes droplet collision under action of forced convection. On the other hand, the broad distribution of droplet composition in the two samples has been attributed to different reasons in terms of a difference in the substructures of the droplets. In the $Cu_{75}Co_{25}$ sample, it is mainly due to in situ decomposition of the L_1 droplets during continuous liquid phase separation. In the $Cu_{84}Co_{16}$ sample, it is mainly due to asynchronous crystallization of the L_1 droplets.

Acknowledgements This work is financially supported by the Fundamental Research Funds for the Central Universities under grant Nos. N090109001 and N100309001. Part of work is supported by the Deutsche Forschungsgemeinschaft within grant HE1601/22-1.

References

1. Nakagawa Y (1958) Acta Metall 6:704
2. Ratke L, Diefenbach S (1995) Mater Sci Eng Rep 15:263
3. Elder SP, Munitz A, Abbaschian GJ (1989) Mater Sci Forum 50:137
4. Munitz A, Abbaschian R (1991) J Mater Sci 26:6458. doi: 10.1007/BF00551897
5. Munitz A, Elder-Randall SP, Abbaschian R (1992) Metall Trans A 23:1817
6. Munitz A, Abbaschian R (1996) Metall Mater Trans A 27:4049
7. Song X, Mahon SW, Cochrane RF, Hickey BJ (1997) Mater Lett 31:261
8. Li D, Robinson MB, Rathz TJ, Williams G (1998) Mater Lett 36:152
9. Yamauchi I, Ueno N, Shimaoka M, Ohnaka I (1998) J Mater Sci 33:371. doi:10.1023/A:1004319829612
10. Munitz A, Abbaschian R (1998) J Mater Sci 33:3639. doi: 10.1023/A:1004663530929
11. Robinson MB, Li D, Rathz TJ, Williams G (1999) J Mater Sci 34:3747. doi:10.1023/A:1004688313591
12. Cao CD, Letzig T, Görler GP, Herlach DM (2001) J Alloys Compd 325:113
13. Sun Z, Song X, Hu Z, Yang S, Liang G, Sun J (2001) J Alloys Compd 319:266
14. Cao CD, Görler GP, Herlach DM, Wei B (2002) Mater Sci Eng A 325:503
15. Cao B, Wei DM, Herlach J (2002) Mater Sci Lett 21:341
16. Cao CD, Herlach DM, Kolbe M, Görler GP, Wei B (2003) Scr Mater 48:5
17. Lu XY, Cao CD, Kolbe M, Wei B, Herlach DM (2004) Mater Sci Eng A 375–377:1101
18. Palumbo M, Curiotto S, Battezzati L (2006) Calphad 30:171
19. Curiotto S, Pryds NH, Johnson E, Battezzati L (2006) Metall Mater Trans A 37:2361
20. Battezzati L, Curiotto S, Johnson E, Pryds NH (2007) Mater Sci Eng A 449–451:7
21. Curiotto S, Pryds NH, Johnson E, Battezzati L (2007) Mater Sci Eng A 449–451:644
22. Yasuda H, Ohnaka I, Ninomiya Y, Ishii R, Fujita S, Kishio K (2004) J Cryst Growth 260:475
23. Kolbe M, Gao JR (2005) Mater Sci Eng A 413–414:509
24. Zhang YK, Gao J, Nagamatsu D, Fukuda T, Yasuda H, Kolbe M, He JC (2008) Scr Mater 59:1002
25. Gao J, Zhang YK, Fukuda T, Yasuda H, Kolbe M, He JC (2009) J Phys Conf Ser 144:012117
26. Antion C, Chatain D (2007) Surf Sci 601:2232
27. Dong C, Wei B, Leonhardt M, Lindenkreuz HG, Löser W (1998) Inter J Non Equil Process 10:241